Pergamon

Int. J. Heat Mass Transfer. Vol. 39, No. 8, pp. 1649–1663, 1996
Copyright © 1996 Elsevier Science Ltd
Printed in Great Britain. All rights reserved
0017–9310/96 $15.00+0.00

0017–9310(95)00256–1

Experimental study of unstable mixed convection of air in a bottom heated horizontal rectangular duct

W. L. LIN and T. F. LIN†

Department of Mechanical Engineering, National Chiao Tung University, Hsinchu, Taiwan, Republic of China

(*Received* 5 *January* 1995 *and in final form* 28 *June* 1995)

Abstract—An experiment was carried out to investigate the buoyancy induced spatial and temporal flow transition and the associated heat transfer processes in a mixed convective air flow through a bottom heated horizontal rectangular duct, by measuring the local heat transfer coefficient, spanwise temperature distributions, air temperature variation with time at selected locations and by visualizing the cross plane secondary flow for the Reynolds numbers ranging from 9 to 186 and the Grashof numbers up to 5×10^6. The results indicated that the heat transfer enhancement is due to the formation and development of a buoyancy driven secondary vortex flow. The onset of thermal instability was found to move upstream for a higher Grashof number and to be delayed for a larger Reynolds number. At increasing Grashof numbers the measured spanwise time-averaged fluid temperature distributions and the corresponding instantaneous flow visualizations clearly show the formation of secondary vortex flow and the changes in the flow structures. At slightly supercritical Grashof numbers, the secondary flow is in the form of two pairs of longitudinal rolls with the vortex flow ascending along the side walls. For higher Grashof numbers the vortex rolls rotate in opposite directions, with the secondary flow descending near the side walls. At even higher Grashof numbers, merging of the vortices takes place and only one pair of vortex rolls exist. Furthermore, raising the Grashof number or lowering the Reynolds number causes the flow to change from a laminar time periodic to a transitional quasiperiodic and even to a chaotic turbulent state. Based on the present data, a regime map delineating the temporal state of the flow and a correlating equation for the Hopf bifurcation were proposed.

1. INTRODUCTION

A mixed convective flow in a bottom heated rectangular duct is simple and steady when the buoyancy is small compared with the inertia. But when the buoyancy is dominated over the inertia, the flow can become unsteady, transitional and even turbulent. Additionally, various complex flow structures like the longitudinal vortices, transverse waves and flow reversal may appear during this buoyancy induced flow transition. These complicated processes are often encountered in a low Reynolds number flow. Detailed understanding of these buoyancy induced flow transition processes is important in fundamental fluid mechanics and heat transfer study and in various technological processes, such as the cooling of microelectronic equipments [1], heat transfer in compact heat exchangers [2], growth of single crystal through chemical vapor deposition [3] and many others. In particular for CVD, reactors are operated with a combination of large Grashof number (*Gr*) and small Reynolds number (*Re*) so that the value of Gr/Re^2 ranges from 10 to 1000. The superposition of transverse and longitudinal vortices can lead to rather non-uniform deposition layer thickness. But how the governing parameters affect these processes is still poorly understood. In the following, the relevant literature is briefly reviewed.

The onset of the thermal instability and the associated heat transfer enhancement in a bottom heated horizontal plane channel was found to occur at $Ra = 1708$, as predicted from experimental measurements [4–9] and linear stability theory [4]. Beyond this critical Rayleigh number, steady longitudinal vortex rolls prevail. Ostrach and Kamotani [6, 7] experimentally noted that the vortex rolls become irregular as $Ra > 8000$. In the thermal entrance region Kamotani *et al.* [9] indicate that the heat transfer rate is affected not only by the Rayleigh number but also by the buoyancy-to-inertia force ratio Gr/Re^2. In the mixed convection of nitrogen gas, Rosenberger and his coworkers [10, 11] observed the unsteady snaking longitudinal vortex rolls even for the Rayleigh number only slightly above the critical value of 1708. Besides, the asymmetric roll patterns were found also at low Rayleigh numbers. A flow regime map of *Re* vs *Ra* was proposed to predict the boundaries among the flow with no roll, steady and unsteady rolls. Finally, the transverse rolls were noted at very low Reynolds number by Ouazzani *et al.* [12, 13]. They also refined the regime map to include the transverse rolls.

---

† Authors to whom correspondence should be addressed.

NOMENCLATURE

A	aspect ratio, b/d
A_{side}	area of the side wall
A_t	area of the top wall
A_w	area of the heated plate
b, d	width and height of the duct
F	shape factor
g	gravitational acceleration
Gr	modified Grashof number, $g\beta q''_{conv} d^4/k\nu^2$
h	local convection heat transfer coefficient
I	electric current
k	thermal conductivity
L	length of the heated plate
M	volume flow rate
Nu	Nusselt number, hd/k
Pr	Prandtl number, ν/α
Q''_{tot}	the total heat dissipation in the plate
q''_{conv}	local convective heat flux
q''_{insul}	local conduction heat loss through the insulation
q''_{loss}	local heat loss, $q''_{rad}+q''_{insul}$
q''_{rad}	local radiation heat loss from the surface
q''_{tot}	the total heat flux in the plate
Ra	Rayleigh number
Ra^*_c	critical Rayleigh number
Re	Reynolds number, $\bar{w}_{in}d/\nu$
t	time
T	temperature
T_{avt}	time average temperature at a given location
T_b	bulk temperature
u, v, w	velocity components in x, y, z directions
V	voltage
x, y, z	Cartesian coordinates
X, Y, Z	dimensionless Cartesian coordinates, x/d, y/d and z/d
Z^*_c	critical modified Z coordinate, $Z/(Re \times Pr)$.

Greek symbols

α	thermal diffusivity
β	thermal expansion coefficient
ε	emissivity
ν	kinematic viscosity
ρ	density
σ	Stefan–Boltzmann constant.

Subscripts

in	values at the inlet of the test section
side	of side wall qualities
t	of top wall qualities
w	of heated wall qualities.

Superscripts

$^-$	average value.

A series of experiments have been conducted by Incropera and his coworkers [14–19] to investigate buoyancy effects on a forced air or water flow in a horizontal plane duct with the bottom and/or top plates subject to uniform heat fluxes. The onset and qualitative picture of the buoyancy driven secondary flow on the bottom plate were clearly visualized [14]. While over the top plate the buoyancy shows little effect in the laminar flow, but it results in relaminarization in the transitional and turbulent flows [15]. Their flow visualization distinctly discloses four flow regimes along the bottom plate–laminar forced convection, laminar mixed convection, transitional mixed convection and turbulent free convection. The transition to turbulent flow was attributed to the breakdown of the vortices due to the hydrodynamic instability [17].

Various numerical works [20–36] were carried out on the basis of the assumption that the axial viscous and thermal diffusion can be neglected, i.e. the flow is parabolic and thus the problem can be solved efficiently by various marching techniques. In view of the presence of the three-dimensional transient transitional flow in the duct, this approximation becomes inappropriate at high Rayleigh or low Reynolds numbers. To explore the buoyancy induced flow transition in low Reynolds number flow, recently Huang and Lin [37] directly solved the unsteady three-dimensional elliptic flow equations by a higher order finite difference numerical scheme, without using any turbulence modeling for $Re = 500$ and $A = 2$. They revealed that the buoyancy induced laminar to turbulent flow transition follows the Ruelle–Taken route. This remains to be verified by experiments.

In may cases such as the practical CVD reactors it is necessary to consider the effects of the aspect ratio of the channel on the unstable mixed convection. Moffat and Jensen [38, 39] suggested that the buoyancy driven secondary flow structure is very sensitive to the aspect ratio and needs to be investigated in detail. To complement our previous numerical analysis [37], the present experiments are intended to measure the characteristics of the flow transition and the associated changes in the secondary flow structure, and heat transfer in the mixed convective air flow in a bottom heated horizontal rectangular duct of a finite aspect ratio ($A = 4$). Attention is focused on the effect of the Grashof and Reynolds numbers on the transitional flow characteristics. Specifically, an experiment is designed to detect the flow transition by examining

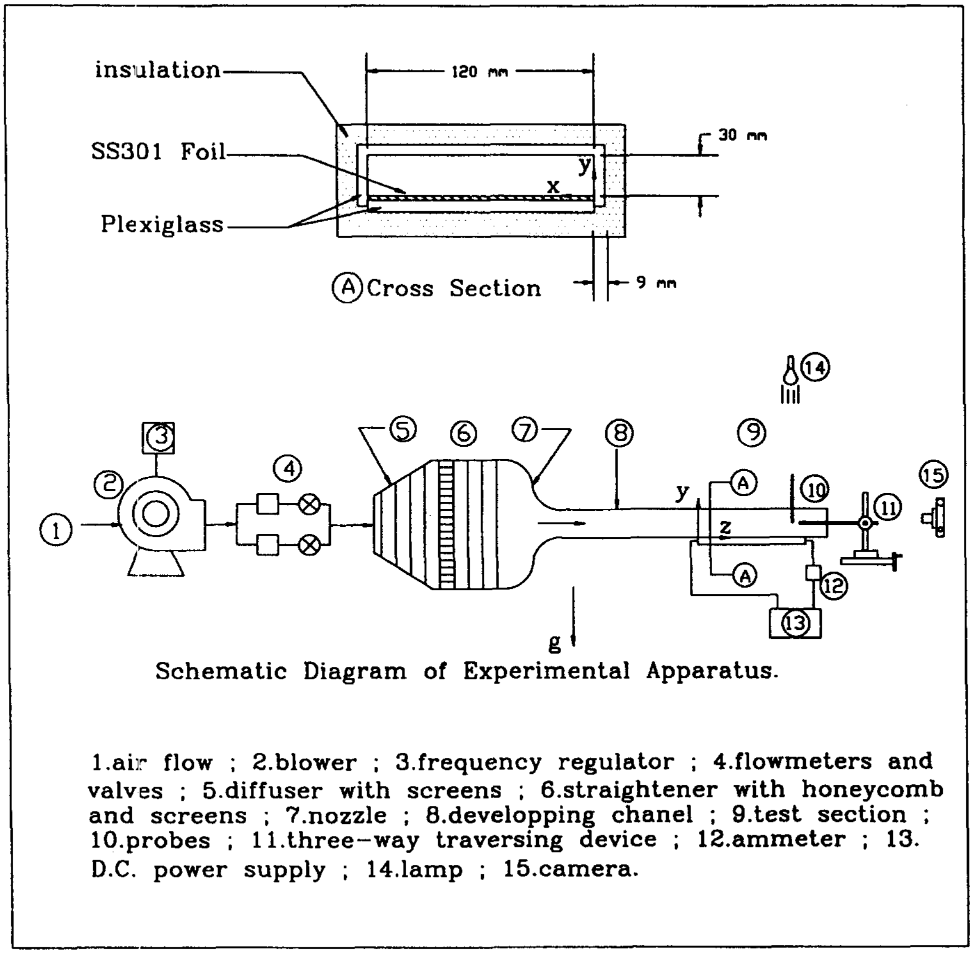

Fig. 1. The schematic diagram of the experimental apparatus.

the local temperature variations with time at selected detection points and to visualize the flow structure at relatively large Gr/Re^2.

2. EXPERIMENTAL APPARATUS AND PROCEDURES

2.1. *Experimental apparatus*

Figure 1 shows a schematic view of the mixed convective experimental apparatus established in this study. The apparatus consists of three parts: wind tunnel, test section and measuring probes along with the data acquisition system. The test section is a bottom heated rectangular duct constructed of 9 mm thick plexiglass top and side walls to facilitate flow visualization. The cross-section of the duct is rectangular, 30 mm in height and 120 mm in width, providing an aspect ratio of $A = 4$ and a total length of $L = 800$ mm. Its bottom wall was made of 0.25 mm thick SS301 stainless steel heater plate, 120 mm wide by 800 mm long, and is bonded to a sheet of 12 mm thick plexiglass plate. Direct electric current was provided from a 30V–50A d.c. power supply and transferred to the heater plate through several copper bus-bars firmly attached at the ends of the heater, intending to produce a nearly uniform heat flux boundary condition. Power dissipation was determined by measuring the current and voltage drop across the heater plate and uniformity of the energy dissipation was checked by measuring the voltage distribution on the plate. Specifically. The longitudinal measurements yield a linear voltage drop and spanwise measurements resolve variations no larger than 0.3 mV for a voltage drop of 0.418 V across the heater plate in the pure natural condition at high wall heat flux. The total heat dissipation in the plate is

$$Q''_{\text{tot}} = I \times V, \tag{1}$$

where I is the electric current and V is the electric voltage drop across the plate. To measure the d.c. current past through the heater plate, a d.c. ammeter (YOKOGAWA model 201137) is arranged in series connection with the plate. The accuracy of the ammeter is within 0.01A. To determine the voltage drop across the heater plate, a digital multimeter (Chung 6005) with an accuracy of 0.01 mV is employed to measure the voltage difference between two ends of the heater plate. The entire channel, including the test section and the upstream and downstream flow straighteners, was insulated with the Superlon insulator of 150 mm thick and mounted on a rigid supporting flame.

The working medium was air which was driven by a blower and sent into the long rectangular duct downstream of a diffuser buffer section, as shown in Fig. 1. The flow rate is controlled by a variable speed blower whose speed is controlled by an a.c. motor with an output frequency of 0–60 HZ. The volume flow rate of air upstream of the diffuser buffer section was measured by a float-area-type flowmeter with an accuracy of 1.6%. To reduce the influence of the vibration from the blower, a flexible connection made of cloth is used to connect the blower and a diffuser buffer section. The purpose of installing the diffuser buffer section and a series of three additional fine-mesh screens is to reduce turbulence from the blower blades. In the inlet section turbulence was further suppressed by passing the air through a section packed with plastic straws of 3 mm in diameter and bounded on each side by two fine mesh screens, and then followed by a nozzle and a developing channel, before entering the test section. The nozzle is made of 5 mm thick acrylic plate with a contraction ratio of 10 : 1 and has been designed to eliminate flow separation, minimize turbulence, and provide a nearly uniform velocity profile at the inlet of the developing section. The developing section is 1000 mm in full length, approximately 33 times that of the duct height. This ensures the flow is fully developed at the inlet of the test section for $Re \leqslant 200$. An outlet section was added to the test section to reduce the effects of the disturbances from the ambient surrounding of the open-loop wind tunnel on the flow in the test section. The optical observations of the flow structure were performed using smoke tracers to determine the pattern of the secondary flow. A thin sheet of smoke was injected into the test section along the bottom of the channel through a slot across the width of the heater plate just in front of the test section. When illuminated through the top wall by lamps and viewed from the end of the channel, a sharp contrast could be achieved between the channel walls and the smoke.

In order to obtain adequate resolution of the temperature distributions on the bottom wall, the heater plate was instrumented with 57 (placed at 19 longitudinal locations) calibrated copper–constantan (T-type) thermocouples and their signals were recorded by the Hewlett-Packard 3852A data acquisition system with a resolution of ± 0.05°C. Additional thermocouples were used to measure the temperatures of the inlet and outlet air and the top and side plates, and to determine temperature differences across the Superlon insulation underneath the heater plate. A T-type thermocouple having a bead of 70 μm diameter was used to measure the air temperature in the duct, which was equipped in the flow so as to have its sensing point 5 mm upstream of the supporting stainless steel pipe of 1 mm outer diameter. This probe was inserted into the flow through the top wall or from the exit end of the channel and can be traversed in the flow to measure the time-averaged temperature field and the instantaneous temperature. The temperature data are recorded when the system reaches steady or statistical state, usually 5–6 h after starting the test. The experiment was performed mainly at the Grashof numbers ranging from 10^4 to 5×10^6 and for Reynolds numbers below 200. The resulting Gr/Re^2 ratio, which governs the characteristics of a combined free and forced convection in duct flow, was above 2.

2.2. *Data reduction for heat transfer coefficient*

The spanwise-averaged Nusselt number defined as

$$Nu_z = \frac{hd}{k} = \frac{q''_{\mathrm{conv}} d}{(\bar{T}_{\mathrm{w}} - T_{\mathrm{in}})k} \tag{2}$$

is obtained from measuring the local mean bottom wall temperature $\bar{T}_{\mathrm{w}}$ and local convective heat flux q''_{conv}. Note that the above heat transfer coefficient h is based on $(\bar{T}_{\mathrm{w}} - T_{\mathrm{in}})$ instead of $(\bar{T}_{\mathrm{w}} - T_{\mathrm{b}})$ since the heated section is not long ($L/d = 26.7$), so that the convective heat transfer in it is mainly in the entrance region. The surface energy balance relating the total energy dissipated in the heater plate due to electric resistance heating per unit surface area q''_{tot} to the heat fluxes associated with the convection from the surface to the flow q''_{conv}, net radiation heat loss from the surface q''_{rad} and conduction loss through the insulation q''_{insul} is

$$q''_{\mathrm{tot}} = q''_{\mathrm{conv}} + q''_{\mathrm{rad}} + q''_{\mathrm{insul}}. \tag{3}$$

The convective heat flux is therefore determined by measuring the total dissipated heat flux and applying appropriate correlations for the nonconvective components. An implication of the expression in equation (3) is that although uniform heat generation q''_{tot} is achieved in the heated plate, variations in the radiation and conduction losses induce nonuniformities in the convective heat flux. The variations were estimated to be less than 20% of the average q''_{conv}.

Considering the shape factor and surface resistances for thermal radiation from the heated bottom surface to the top surface in a rectangular duct and that from the bottom surface to the two side plates, the net radiation loss from the bottom surface is estimated as

$$\begin{aligned} q''_{\mathrm{rad}} &= \frac{\sigma(\bar{T}^4_{\mathrm{w}} - \bar{T}^4_{\mathrm{t}})}{\dfrac{1-\varepsilon_{\mathrm{w}}}{\varepsilon_{\mathrm{w}}} + \dfrac{1}{F_{\mathrm{w}\to\mathrm{t}}} + \dfrac{1-\varepsilon_{\mathrm{t}}}{\varepsilon_{\mathrm{t}}\left(\dfrac{A_{\mathrm{t}}}{A_{\mathrm{w}}}\right)}} + 2 \\ &\quad \times \frac{\sigma(\bar{T}^4_{\mathrm{w}} - \bar{T}^4_{\mathrm{side}})}{\dfrac{1-\varepsilon_{\mathrm{w}}}{\varepsilon_{\mathrm{w}}} + \dfrac{1}{F_{\mathrm{w}\to\mathrm{side}}} + \dfrac{1-\varepsilon_{\mathrm{side}}}{\varepsilon_{\mathrm{side}}\left(\dfrac{A_{\mathrm{side}}}{A_{\mathrm{w}}}\right)}} \\ &= 0.331\sigma(\bar{T}^4_{\mathrm{w}} - \bar{T}^4_{\mathrm{t}}) + 2 \times 0.082\sigma(\bar{T}^4_{\mathrm{w}} - \bar{T}^4_{\mathrm{side}}), \end{aligned} \tag{4}$$

where

$$\varepsilon_w \approx 0.39 \quad \varepsilon_t = \varepsilon_{side} \approx 0.85$$

$$F_{w\to t} \approx 0.78 \quad F_{w\to side} \approx 0.1$$

$$A_t/A_w = 1 \quad A_{side}/A_w = 0.25.$$

The mean temperature of the heated surface $\bar{T}_w$ is measured directly, and the mean top(side) plate temperature $\bar{T}_t(\bar{T}_{side})$ is obtained by interpolation between the measured values. Radiation losses were estimated to range from 24 to 33% of the total flux.

Conduction losses through the insulation q''_{insul} were calculated by assuming one-dimensional conductive transfer and by measuring the temperature difference across the first 9 mm of the insulation ($k_{insul} = 0.21$ W m^{-1} °C^{-1}) beneath the heater plate. Losses calculated in this manner were estimated to range from 14 to 23% of the total flux q''_{tot},

$$q''_{insul} = -k_{insul}\left.\frac{\Delta T}{\Delta y}\right|_{insul}. \tag{5}$$

2.3. *Analysis of temperature fluctuation*

The time-averaged temperature and the intensity of the temperature fluctuation of the air flow were obtained by averaging 1000 sampled data at each detection point. In the tests, the detection points are distributed at 24 equi-spaced spanwise positions in the horizontal planes at $y = 5$, 15 and 25 mm. Also, the power spectrum densities of the temperature fluctuation were obtained by analyzing the output of the thermocouple using a FFT analyzer. The response time of the thermocouple is about 0.13 s.

3. EXPERIMENTAL RESULTS AND DISCUSSIONS

3.1. *Preliminary investigation of flow field*

In order to confirm the fully developed laminar flow at the inlet of the heated test section, the cross-sectional velocity distributions were measured in the entrance region of the test section using a hot-wire probe which was operated by a constant temperature anemometer (DANTEC Probe Type 55P11 with 56C17 CTA Bridge). For calibrating the hot-wires, the pipe-flow method, where the probe is placed in the center of a fully developed laminar pipe flow, was used. The total flow rate is measured and the pipe center velocity is calculated from the parabolic distribution. Figure 2 shows the measured velocity profiles along the vertical centerline at $x = 60$ mm and horizontal centerline at $y = 15$ mm for $Re = 186$ with no heat input to the bottom plate. These results are in good agreement with the analytical results given by Shah and London [40]. The turbulence level of the inlet stream also given in the figure is all within 1%, implying that the effects of the free stream turbulence on the mixed convective flow characteristics are moderate.

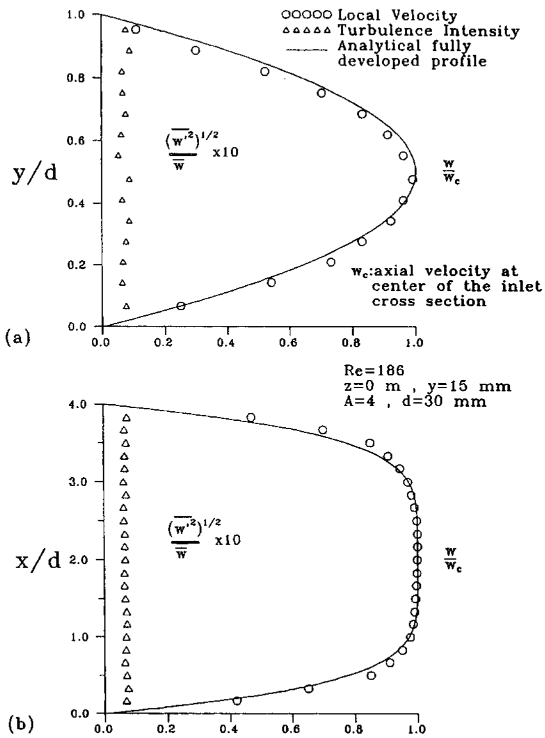

Fig. 2. Fully developed velocity distribution at the inlet of heated section for $Pr = 0.72$ and $Re = 186$ for (a) along the vertical centerline at $x = 60$ mm and (b) along the horizontal centerline at $y = 15$ mm.

3.2. *Heat transfer coefficient*

Uncertainties in the Nusselt number and other parameters were estimated according to the standard procedures proposed by Kline and McClintock [41]. Our analysis indicated that the combination of many measurements, together with the uncertainties in the predicted quantities (radiation and conduction losses), yields the Nusselt number uncertainties ranging from 4 to 10%. Uncertainty in the Grashof number ranges from 10 to 25%, which primarily reflects the uncertainty in the convective heat flux. The estimated uncertainty in the Reynolds number was 2%. Because of the fluid property variations with the temperature the Reynolds and Grashof numbers vary with axial distance. Although the variations in the Reynolds number were small, the Grashof number could vary by as much as 25%. For convenience, experiments are identified according to the Reynolds and Grashof numbers based on the inlet conditions and averaged convection heat flux. The uncertainties of various parameters are summarized in Table 1.

The reliability of the present data of the spanwise-averaged Nusselt number was established through various tests and comparison with some appropriate standard conditions. The most relevant comparison is to compare the measured data for small Grashof numbers with the numerical solution for the corresponding forced convection. This comparison is made in Fig. 3. The agreement with the numerical

Table 1. Summary of the uncertainty analysis

Parameters and estimated uncertainties Parameter	Uncertainty
L, b, d (m)	± 0.0005 m
T_{in} [°C]	± 0.2°C
T_{w}, T_{t}, T_{side} [°C]	± 0.15°C
I [Amp]	$\pm 1.5\%$
V [Volt]	$\pm 1.5\%$
M [L min^{-1}]	$\pm 1.6\%$
k_{f} [W(K m)$^{-1}$]	$\pm 0.05\%$
μ [$N \cdot$m s^{-2}]	$\pm 0.05\%$
ρ [kg m^{-3}]	$\pm 0.05\%$
ν [m^2 s^{-1}]	$\pm 0.07\%$
$(\bar{T}_{\mathrm{w}} - T_{\mathrm{in}})$ [°C]	± 0.25°C
Q''_{tot} [W]	$\pm 2.12\%$
q''_{tot} [W m^{-2}]	± 14.8 [W m^{-2}]
$q''_{\mathrm{rad,t}}$ [W m^{-2}]	± 0.57 [W m^{-2}]
$q''_{\mathrm{rad,s}}$ [W m^{2}]	± 0.48 [W m^{-2}]
q''_{insul} [W m^{-2}]	± 6.1 [W m^{-2}]
q''_{loss} [W m^{-2}]	± 6.12 [W m^{-2}]
q''_{conv} [W m^{-2}]	± 16 [W m^{-2}]
Gr	$\pm 10 \sim 25\%$
Re	$\pm 2.04\%$
Gr/Re^2	$\pm 10.5 \sim 25.2\%$
Nu	$\pm 4 \sim 10\%$

prediction [37] is excellent and well within the experimental uncertainty.

As the heat flux is increased beyond certain critical value depending on Re, the Nusselt number exhibits a discernible departure from the forced convection limit indicating the onset of the longitudinal vortex rolls. This is shown in Fig. 4 for the case with $Gr = 1.1 \times 10^5$ and $Re = 102$, and is also compared to the numerical solution and the forced convection result. The agreement is also good, except that the earlier appearance of the vortex rolls is predicted in the numerical study. This difference is attributed to the significant conduction heat transfer from the heated bottom plate to the top plate through the plexiglass side walls whose thermal conductivity is much higher than that of air. This conjugated heat transfer effect was not included in the numerical calculation [37]. Note that the monotonic decay in the Nusselt number associated with the forced convection dominated region ends when the buoyancy force becomes strong enough to destabilize the hydrodynamic boundary layer on the bottom plate. Beyond the onset of instability, plumes of warm fluid rise from the heated surface ascending along the side walls, resulting in a developing secondary vortex flow and the bottom heated plate temperature is reduced by the cool fluid descending from the duct core. Thus, the secondary flow circulation provides an effective mechanism for heat transfer enhancement. As the secondary flow strengthens, the Nusselt number rises well above the forced convection limit. Note that the secondary flow can enhance the heat transfer by as much as 110%, as the Nusselt number rises to its maximum at $z \approx 0.4$ m. Downstream of this location the fluid in the core region has been warmed up by the secondary flow and the descending fluid is no longer at the inlet temperature. Thus the reduction in the surface temperature is less pronounced and the Nusselt number begins to decay. The intensity of the secondary vortex flow can increase with the axial direction, since the flow of air continues to receive heat from the bottom plate as it moves downstream. Thus the Nusselt number can rise with the axial distance. As a result, Nu_z exhibits a wavy variation with z in the downstream region.

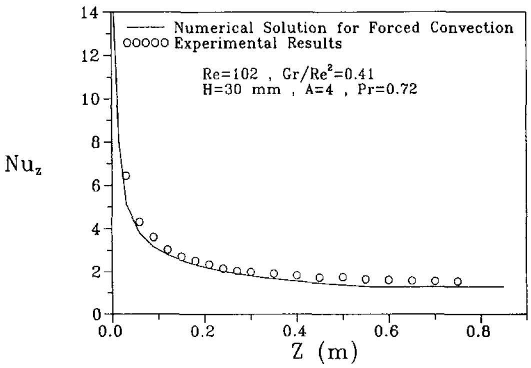

Fig. 3. Comparison of the experimental data with numerical solution for forced convection.

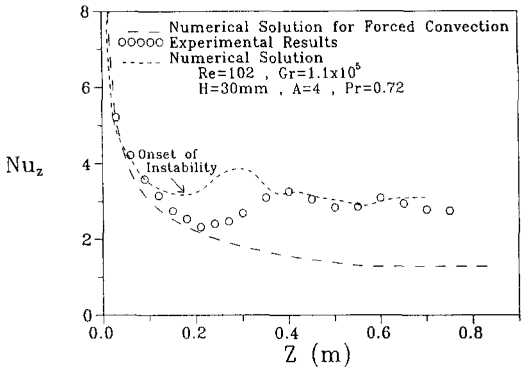

Fig. 4. Comparison of the predicted spanwise-averaged Nusselt number distribution with the measured data for $Re = 102$, $Gr = 1.1 \times 10^5$ and $A = 4$.

The expected spanwise temperature variations on the heated bottom plate caused by the three-dimensional nature of the secondary vortex flow were justified by the present measurements. The local Nusselt number distributions were spanwisely uniform at a given axial position prior to the onset of instability, but certain spanwise variations ($\pm 10\%$) occurred after the formation of the secondary flow. Since a much larger axial change in the Nusselt number following the onset of thermal instability was always accompanied by some spanwise variations, the axial distribution of the local Nusselt number can be well represented by its spanwise average.

Effects of the Grashof number on the spanwise aver-

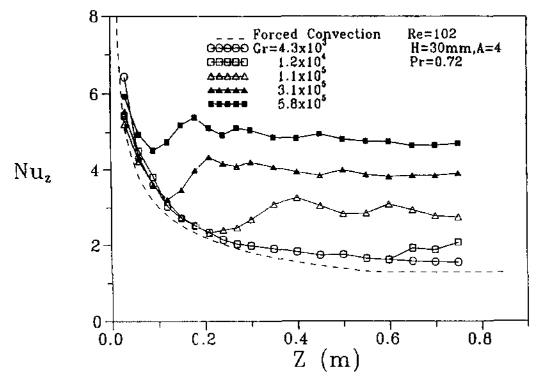

Fig. 5. The spanwise-averaged Nusselt number distributions for various Grashof numbers for $Re = 102$.

aged Nusselt number are discussed first. Figure 5 depicts the Nu_z distribution for $Re = 102$ and Gr varied from 4.3×10^3 to 5.8×10^5. The results indicate that for a given Grashof number each Nu_z curve initially follows the forced convection limit. However, the location at which the heat transfer enhancement begins to be noted advances upstream at increasing Grashof numbers. It is important to note that for a higher Grashof number, there is a greater departure from the forced convection limit before a minimum in the Nusselt number is reached. Beyond this minimum Nu_z location rapid velocity boundary layer growth in the upstream region prevents the secondary flow from fully compensating for the effect of the thickening boundary layer. Hence the Nusselt number, although enhanced above the forced convection limit, continues to decline. They also suggest that the axial oscillations in the Nusselt number will decay to a final fully developed value which increases with the Grashof number.

Next, the effects of the Reynolds number on the Nu_z distributions are examined. Figure 6 demonstrates that an increase in the Reynolds number shifts the onset of instability downstream and reduces the Nusselt number in the downstream region. This effect is expected as the increased flow velocity thins the boundary layer on the bottom plate, thereby increasing its resistance to thermal instability and impeding secondary flow development.

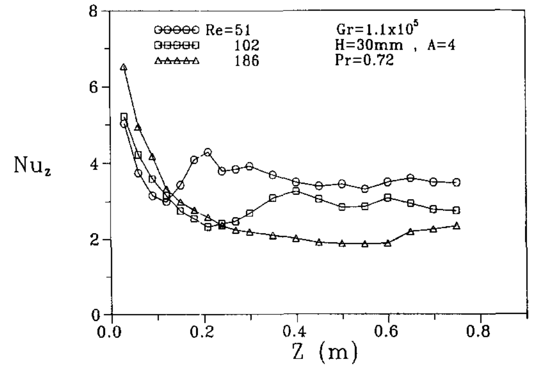

Fig. 6. The spanwise-averaged Nusselt number distributions for various Reynolds numbers for $Gr = 1.1 \times 10^5$.

Finally, the present data for the onset of instability are compared with those in the literature for the mixed convective flow in a horizontal plane channel. The onset point is defined as the location where the heat transfer enhanced by the vortex flow is 5% larger than the forced convection value. The results suggest that the onset of thermal instability is delayed for a finite aspect ratio duct, $A = 4$, considered here [37]. Our instability data can be approximately correlated by the equation

$$Ra_c^* = 1330(Z_c^*)^{-1.34}. \qquad (6)$$

3.3. *Spanwise time-averaged air temperature distributions and flow visualization*

Results for the air temperature variations with the spanwise positions and the flow visualizations can reflect the secondary vortex flow structure, and are to be presented in the following. Figure 7a–d shows the non-dimensional spanwise time-averaged air temperature distributions at $y/d = 0.5$ and $z = 0.7$ m and the corresponding instantaneous snapshot of the secondary vortex flow for several Grashof numbers with Re fixed at 102. The reason for presenting the time average temperature distributions is simply because the flow is time oscillatory at high Grashof numbers. The results for the instantaneous temperature variations will be examined later. At a very low Grashof number (≈ 1600) the spanwise temperature distribution in Fig. 7a is close to that for the fully developed forced convection, implying that the buoyancy effect is extremely small. This flow pattern is confirmed by the corresponding instantaneous flow visualization shown. As the Grashof number is raised to 10^4, significant spanwise temperature variation begins to appear, suggesting the existence of the buoyancy driven vortex flow at the cross-section $z = 0.7$ m. At $Gr = 2.5 \times 10^4$, three peaks appear in the spanwise temperature distribution shown in Figure 7b, one adjacent to the vertical center plane at $x = 60$ mm and another two near the side walls, which result from the presence of two pairs of longitudinal vortex rolls in the duct with the flow ascending along the vertical middle plane and the side walls, as evident from the flow visualization and the corresponding schematically sketched vortices. The slight asymmetry in the spanwise temperature distribution with respect to the vertical central plane is attributed to the experimental disturbances. Similar asymmetry was also found in a longer duct studied by Nyce *et al.*, [42]. As the Grashof number is further raised to 3.1×10^5, two temperature peaks are observed near the vertical center plane (Fig. 7c). This unique temperature distribution is conjectured to result from two pairs of vortices with the upward vortex flow near the peaks and downward flow near the valleys. Note that the induced vortices at this higher Gr rotate in an opposite direction to that in Fig. 7b for $Gr = 2.5 \times 10^4$, with the

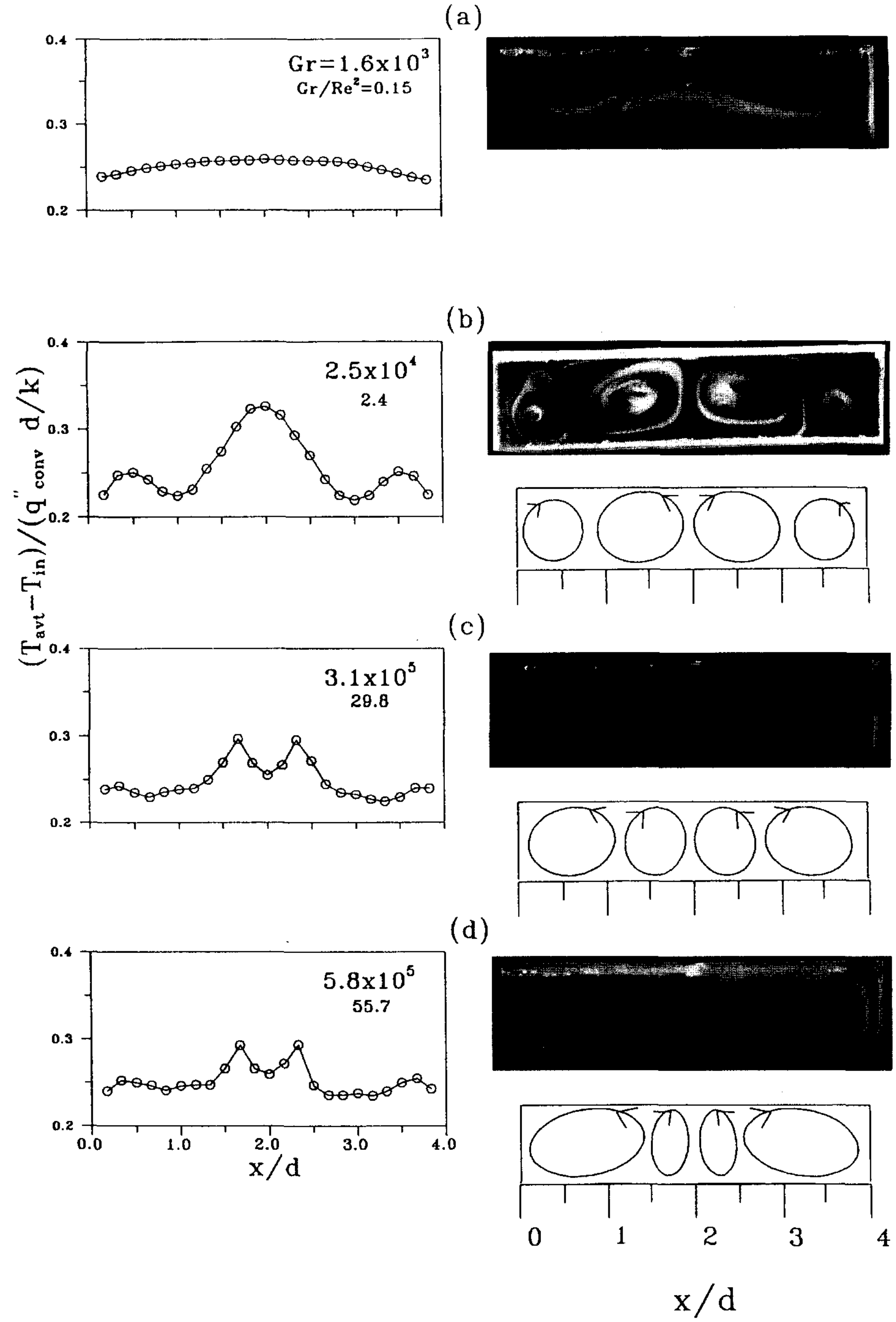

Fig. 7. The time-averaged spanwise temperature distributions at $z = 0.7$ m and $y/d = 0.5$ and the instantaneous flow photos at $z = 0.7$ m for $Re = 102$ and various Grashof numbers.

secondary flow descending along the side walls. These vortices are designated as the 'reverse vortices' which might result from the higher conduction heat transfer through the side walls at higher *Gr*. From the associated flow visualization, two pairs of unsteady longitudinal vortex rolls were observed to swing back and forth in the spanwise direction and slowly change their shape with time, as detected in the time records of the air temperature to be described later. Note that the distance between the two peaks in the duct core is rather small and the induced vortex pair near the vertical center plane $x = 60$ mm is much smaller than the other pair. Similar results are noted in Fig. 7d for an even higher Grashof number ($Gr \approx 5.8 \times 10^5$).

Next, the effects of the Reynolds number are examined. As the Reynolds number is reduced to 51, the

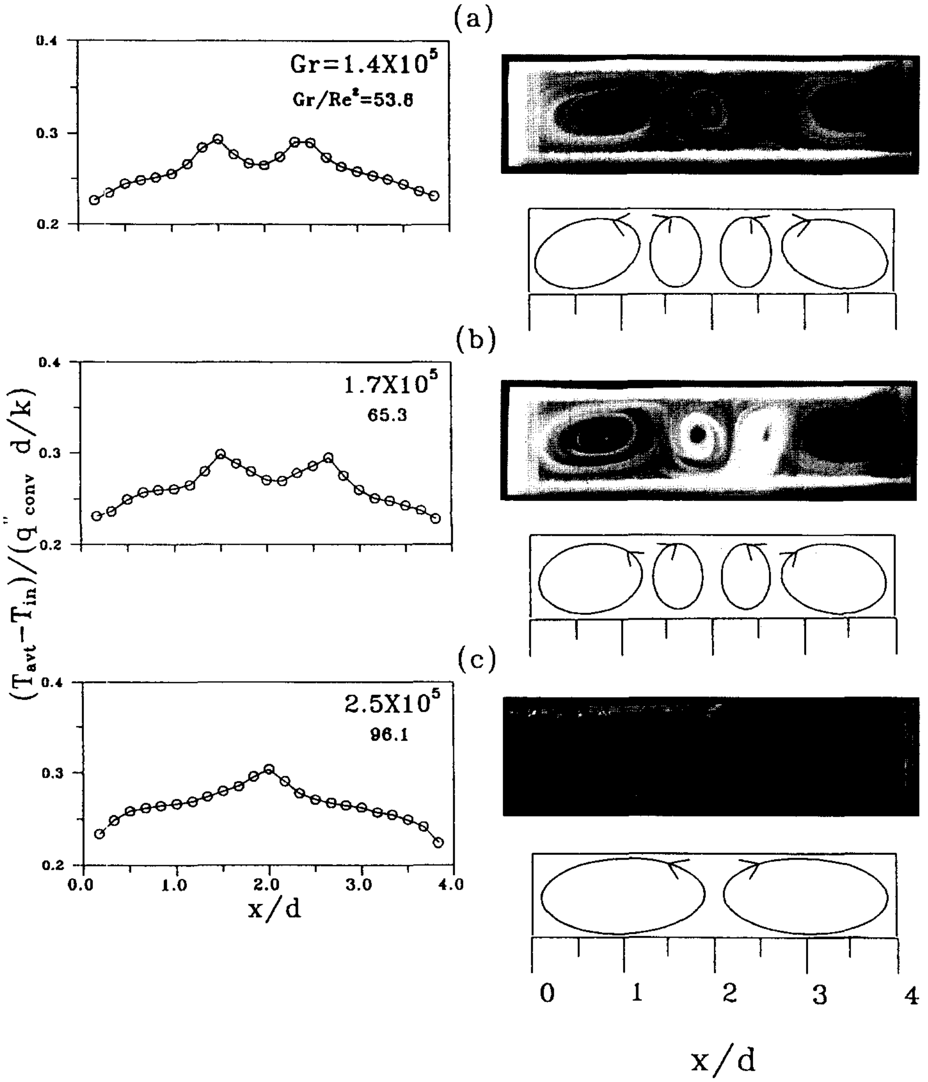

Fig. 8. The time-averaged spanwise temperature distributions at $z = 0.7$ m and $y/d = 0.5$ and the instantaneous flow photos at $z = 0.7$ m for $Re = 51$ and various Grashof numbers.

results from the measurement of the spanwise temperature distributions and flow visualizations for $Gr/Re^2 \leqslant 50$ are qualitatively similar to those for $Re = 102$ in Fig. 7, at the same mixed convection parameter Gr/Re^2. The results for a higher Gr/Re^2 are presented in Fig. 8. Note that for $Gr/Re^2 = 53.8$ and 65.3, the temperature is low near the side walls and two high temperature peaks are observed near the vertical center plane. Thus two pairs of reverse vortices with the downward secondary flow along the side walls are induced. Like those for $Re = 102$ these reverse vortices are also unsteady and, in fact, oscillate periodically in time. At a higher Gr/Re^2 the vortices adjacent to the side walls are bigger. As Gr/Re^2 is further raised over 96.1, there is only one temperature peak in the flow and only one pair of reverse vortices exist in the flow (Fig. 8c). Note that the vortex flow descends near the duct sides and ascends in the core region. The observed vortices are steady at $Gr/Re^2 = 96.1$. This unique secondary flow pattern of one pair of reverse vortices prevails for an even higher buoyancy, but it becomes unsteady for Gr above 2.9×10^5. The above results for $Re = 51$ clearly show the changes in the secondary flow patterns from two pairs of vortices to two pairs of reverse vortices and finally, to one pair of reverse vortices as the buoyancy force is gradually increased.

3.4. *Time records of air temperature and associated power spectrum densities*

Several important flow characteristics can be identified in a mixed convective flow through a bottom heated horizontal duct. The appearance of the secondary vortex flow as the Rayleigh number exceeds the critical value for the onset of instability, is the first unique feature already discussed above. The transition of the steady vortex flow to the unsteady one, the so called 'Hopf bifurcation', at even higher buoyancies

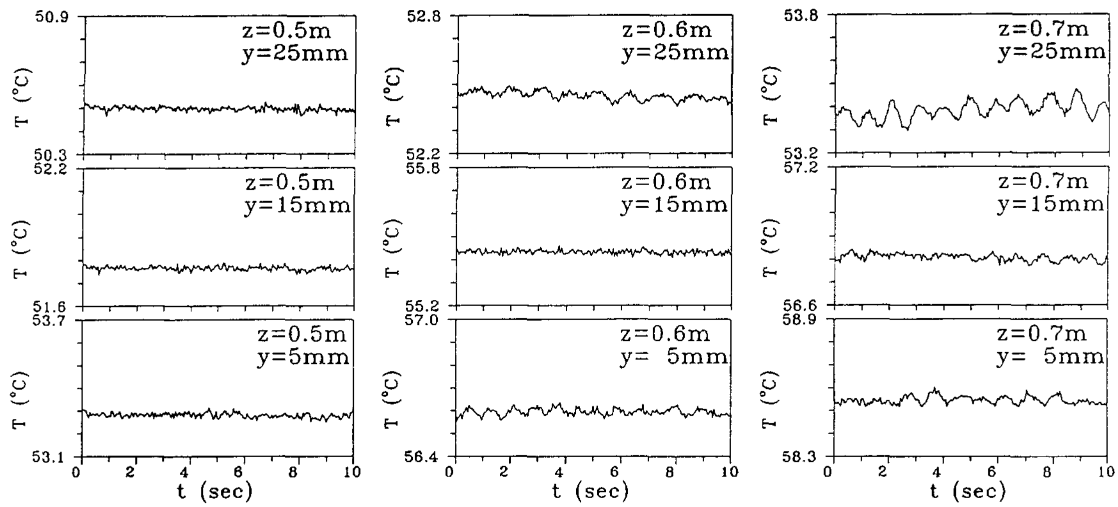

Fig. 9. The time records of the air temperature for $Re = 102$, $Gr = 5.8 \times 10^5$ with $x = 60$ mm and $z = 0.5$, 0.6, 0.7 m at $y = 5$, 15, 25 mm.

is the second important feature to be examined in the following.

Results for the time records of the air temperature at the detection points at $x = 60$ mm and $y = 25$ mm at selected cross sections for $Re = 102$ and $Gr = 5.8 \times 10^5$, indicate that the temperature oscillations for $z \leqslant 0.5$ m are rather small in amplitude and these small amplitude oscillations can be considered to result from the turbulence at the duct inlet. Thus, the temperature at these locations for $z \leqslant 0.5$ m can be regarded as steady. At $z = 0.6$ m the temperature oscillation is quasiperiodic and contains a number of high frequencies, but still in small amplitude. Further downstream at $z = 0.7$ m the temperature is nonperiodic and in a larger amplitude. To investigate the dependence of the temperature oscillation on the axial and vertical positions, Fig. 9 shows the results for the same case with $x = 60$ mm, $z = 0.5$, 0.6 and 0.7 m at $y = 5$, 15 and 25 mm. The results indicate that at $z = 0.5$ m the three temperature traces are steady. A little downstream at $z = 0.6$ m, noticeable quasiperiodic oscillations exist at $y = 5$ and 25 mm. Moving further downstream to the cross-section $z = 0.7$ m, nonperiodic oscillations are seen at all three locations and the oscillation is largest at $y = 25$ mm. Clearly, the oscillations depend on the vertical position to some degree. This finding agrees with the results from numerical simulation [37]. It is also of interest to know the dependence of the temperature on the spanwise position. The results for three spanwise positions, $x = 10$, 60 and 110 mm, at $z = 0.7$ m for the same case are shown in Fig. 10. Note that the temperature oscillation depends slightly on the spanwise position.

Next, the measured time histories of the temperature for various Grashof numbers with the Reynolds number fixed at 102 and 51 at the sampling point, $x = 60$ mm, $y = 25$ mm and $z = 0.7$ m are, respectively, displayed in Figs. 11 and 12. The results indicate that at a very low Grashof number steady temperature is recorded. As the Grashof number exceeds a certain critical value, depending on the Reynolds number, time periodic temperature oscillation is seen. The associated power spectrum densities also given in the figures imply that the temperature oscillation is mainly dominated by a single fundamental frequency. This frequency is not always higher for a higher Grashof number. For a further increase in the Grashof number, a second fundamental frequency appears in the temperature fluctuation indicating the temperature is quasiperiodic. This can be seen in the curve for $Re = 102$ and $Gr = 6.9 \times 10^5$. At an even higher

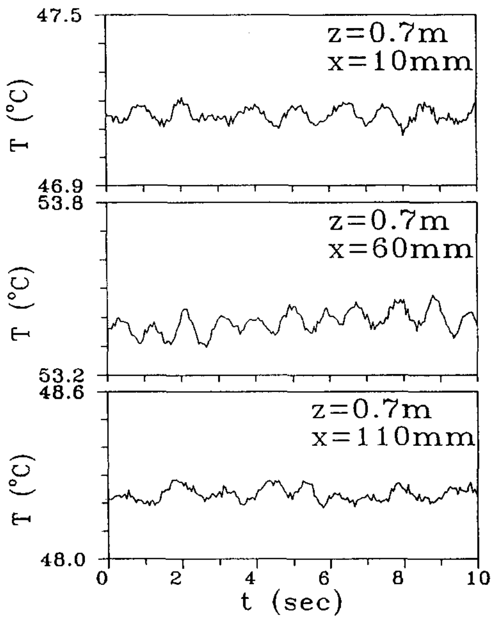

Fig. 10. The time records of the air temperature for $Re = 102$, $Gr = 5.8 \times 10^5$ at $z = 0.7$ m, $y = 25$ mm and $x = 10$, 60, 110 mm.

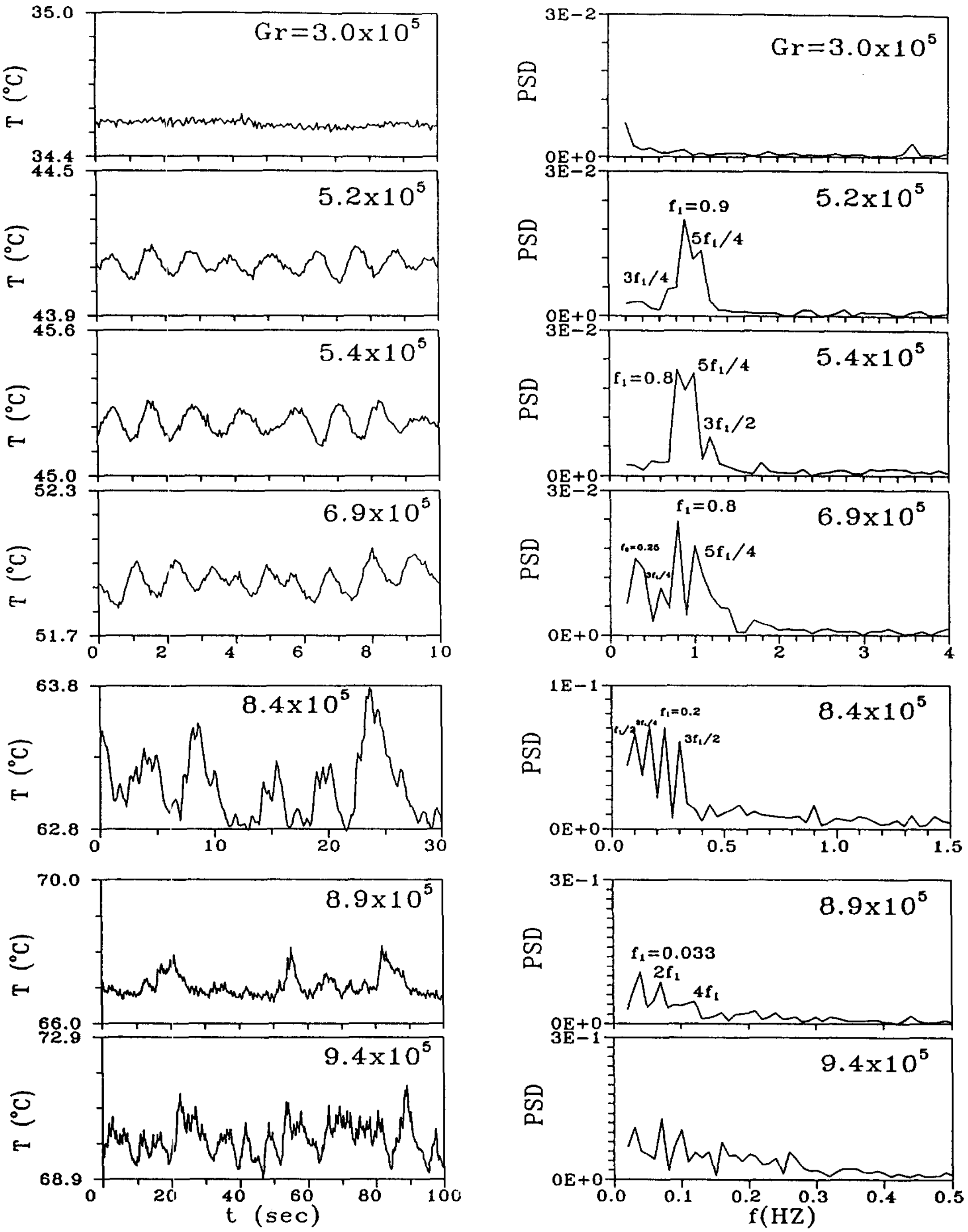

Fig. 11. The time records of the air temperature and the corresponding power spectrum densities for $Re = 102$ and various Grashof numbers at $z = 0.7$ m, $x = 60$ mm and $y = 25$ mm.

Grashof number $Gr \geqslant 7.4 \times 10^5$, irregular temperature oscillations prevail in the flow for $Re = 102$. But for $Re = 51$ the situation is somewhat different. There is a reverse Hopf bifurcation for Grashof number in the range of 1.9×10^5–2.9×10^5. This reverse Hopf bifurcation takes place when there is a corresponding change in the secondary flow patterns from two pairs of reverse vortices, to one pair of reverse vortices shown in Fig. 8b,c. Another reverse transition also tends to occur for $Gr \geqslant 5.5 \times 10^5$ by noting the reduction in the oscillation amplitude at increasing Gr. But since the heated plate temperature is already very close to the design limit of our experimental system at these high Grashof numbers, tests were forced to stop here.

To further illustrate the characteristics of the temperature oscillations, tests were conducted for a fixed Grashof number with the Reynolds number varied.

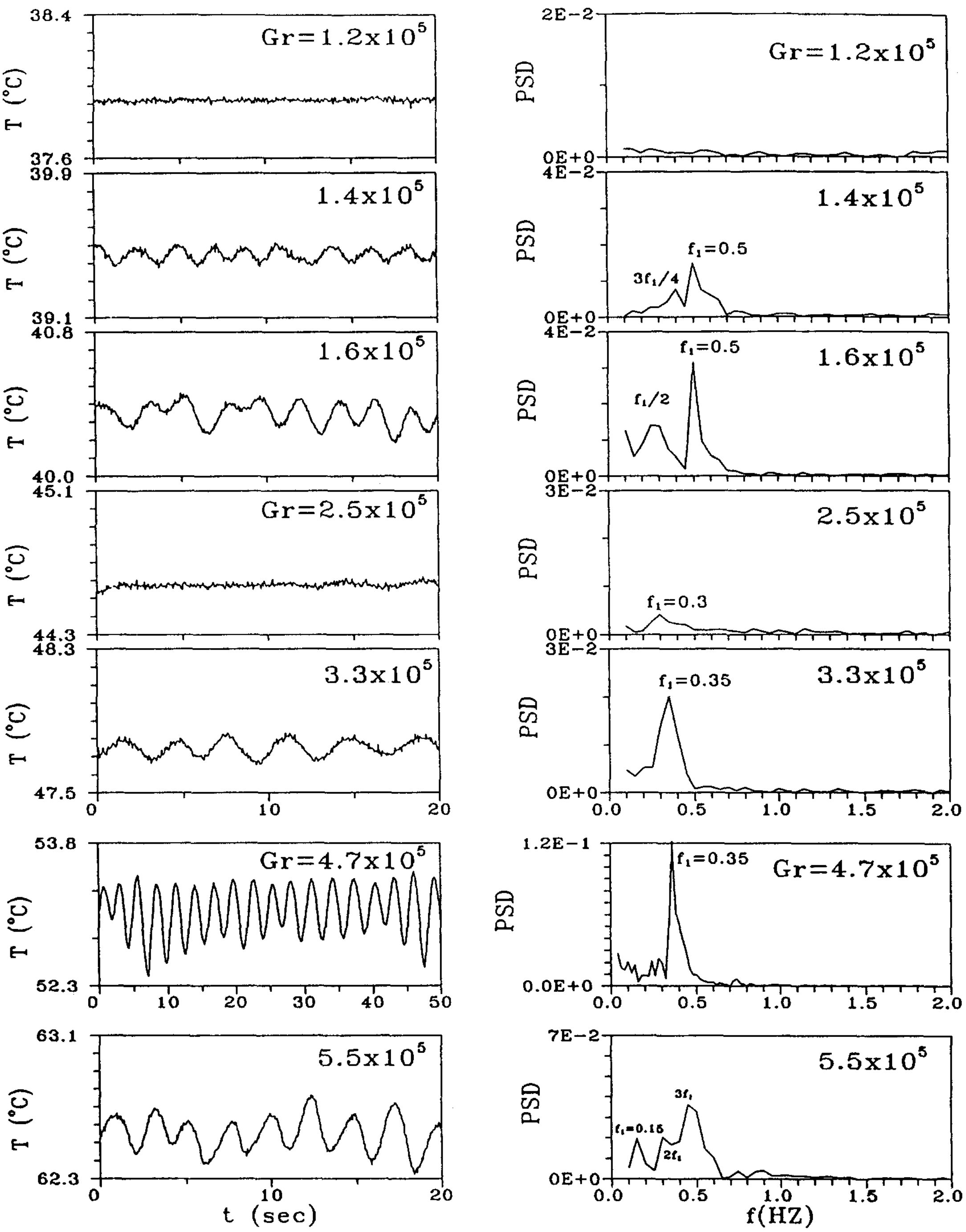

Fig. 12. The time records of the air temperature and the corresponding power spectrum densities for $Re = 51$ and various Grashof numbers at $z = 0.7$ m, $x = 60$ mm and $y = 25$ mm.

First, the temperature traces for $Gr = 8.6 \times 10^4$ at the location $x = 60$ mm, $y = 25$ mm and $z = 0.7$ m with the Reynolds number reduced from 51 to 9 are recorded. All the temperature records were found to be steady. But when the Grashof number is fixed at a higher value of 2×10^5, reducing the Reynolds number from 88 can cause the flow to change from a steady state to a time periodic state for $Re = 44$, 35 and 27 (Fig. 13). Note that the oscillation frequency is lower for a smaller Reynolds number for these three cases. As the Reynolds number is lowered to 22, nonperiodic temperature oscillations appear. At an even low Reynolds number ($= 11$) the temperature fluctuation is irregular. Similar results were obtained for a still higher Grashof number.

Based on the above results for $z = 0.7$ m for various

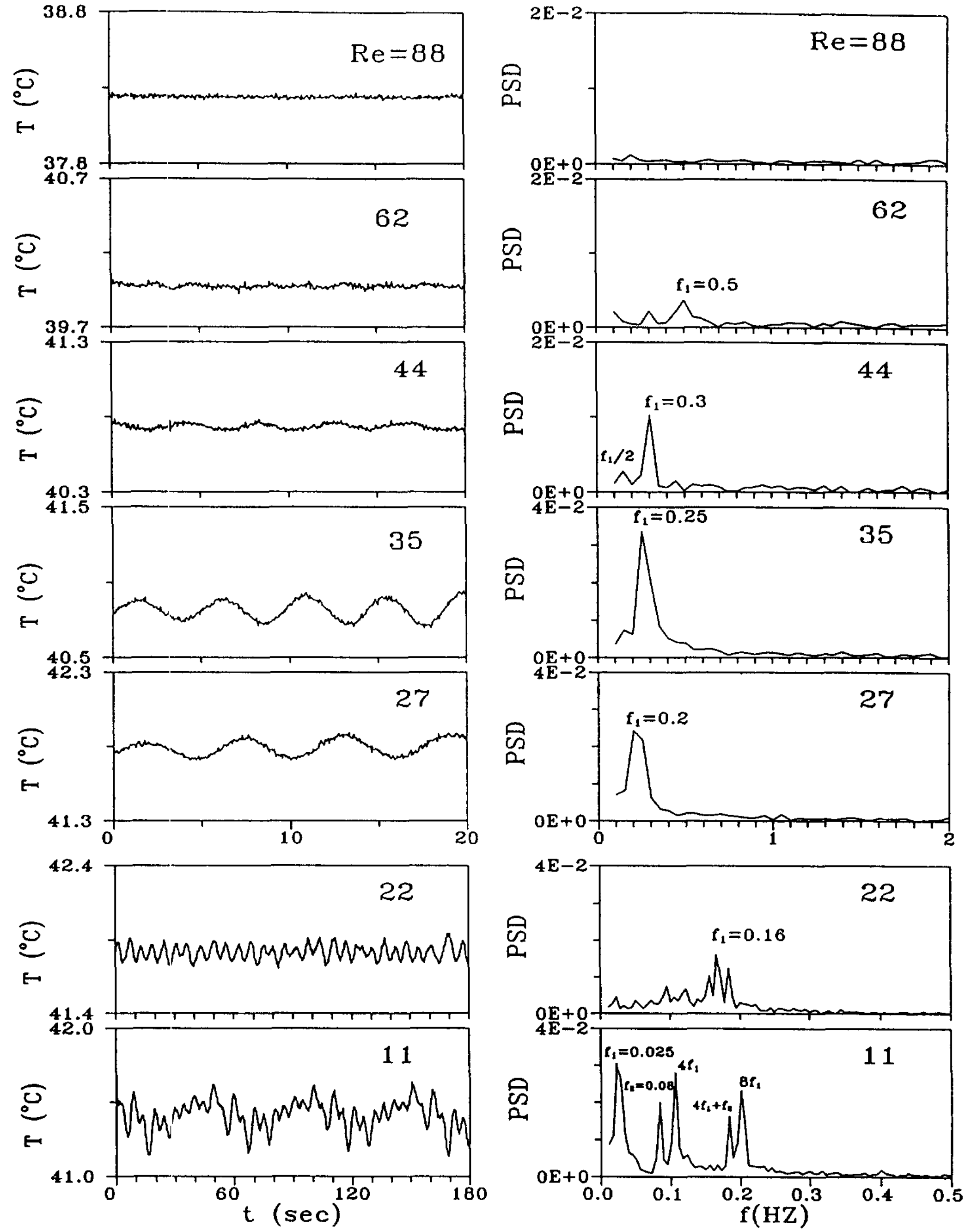

Fig. 13. The time records of the air temperature and the corresponding power spectrum densities for $Gr = 2.0 \times 10^5$ and various Reynolds numbers at $z = 0.7$ m, $x = 60$ mm and $y = 25$ mm.

Reynolds and Grashof numbers, a flow regime map characterizing the temporal state of the flow is given in Fig. 14. The results indicate that the flow is steady at a low Grashof number, beyond a certain critical Grashof number a periodic oscillation is induced, and the oscillation becomes chaotic at a higher Grashof number. For practical use, a correlating equation to fit the boundary between the steady and periodic flow regimes for the present data is proposed,

$$Gr = 200(Re)^{1.6}. \tag{7}$$

4. CONCLUDING REMARKS

We have performed an experimental study concerning the effects of the Reynolds and Grashof numbers on the flow transition in a mixed convective air flow through a bottom heated horizontal rectangular duct, by systematic measurement of the heat transfer coefficient and time records of the air temperature. Additionally, the measurements of the time-averaged spanwise temperature distributions and the instantaneous flow visualizations were also conducted. The

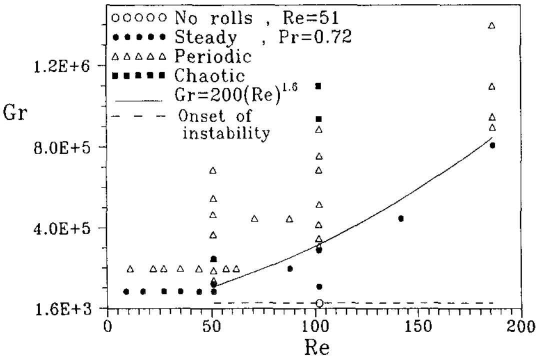

Fig. 14. The flow regime map for various Reynolds and Grashof numbers for *Pr* = 0.72.

experiments were carried out for the Reynolds numbers ranging from 9 to 186 and the Grashof numbers up to 5×10^6. The conclusions obtained are as follows:

(1) In the entry region the upward buoyancy force thickens the thermal boundary layer prior to the onset of thermal instability. The Nusselt number shows a rapid decline with the downstream distance and is slightly smaller than the forced convection limit. Beyond the onset of stability, heat transfer enhancement was attributed to the formation and development of a buoyancy driven secondary vortex flow.

(2) The onset of thermal instability was found to move upstream for increasing Grashof number and decreasing Reynolds number.

(3) Results for the time-averaged air temperature variations with the spanwise positions and the instantaneous flow visualization reflect the secondary vortex flow structure and the temporal state of the flow.

(4) As the Grashof number is high enough, the transition of the steady vortex flow to the time period one, the so called Hopf bifurcation, could occur. Further raising the Grashof number causes the flow to change from a periodic to a quasiperiodic and even to a chaotic state. Similar trends are noted with decreasing Reynolds number. Thus, the flow transition follows the Ruelle–Taken route to chaos. A regime map for characterizing the temporal state of the flow was given and the correlating equation for the Hopf bifurcation was proposed.

Acknowledgement—The financial support of this study by the engineering division of National Science Council of Taiwan, Republic of China through the contract NSC82-0404-E-009-141 is greatly appreciated.

REFERENCES

1. F. P. Incropera, Convective heat transfer in electronic equipment cooling, *J. Heat Transfer* **110**, 1097–1111 (1988).
2. W. M. Kays and A. L. London, *Compact Heat Exchangers* (3rd Edn). McGraw-Hill, New York (1984).
3. G. Evan and R. Grief, A study of traveling wave instabilities in a horizontal channel flow with applications to chemical vapor deposition, *Int. J. Heat Mass Transfer* **32**, 895–911 (1989).
4. Y. Mori and Y. Uchida, Forced convective heat transfer between horizontal flat plates, *Int. J. Heat Mass Transfer* **9**, 803–817 (1966).
5. M. Akiyama, G. J. Hwang and K. C. Cheng, Experiments on the onset of longitudinal vortices in laminar forced convection between horizontal plates, *J. Heat Transfer* **93**, 335–341 (1971).
6. S. Ostrach and Y. Kamotani, Heat transfer augmentation in laminar fully developed channel flow by means of heating from below, *J. Heat Transfer* **97**, 220–225 (1975).
7. Y. Kamotani and S. Ostrach, Effect of thermal instability on thermally developing laminar channel flow, *J. Heat Transfer* **98**, 62–66 (1976).
8. G. J. Hwang and C. L. Liu, An experimental study of convective instability in the thermal entrance region of a horizontal parallel-plate channel heated from below, *Can. J. Chem. Engng* **54**, 521–525 (1976).
9. Y. Kamotani, S. Ostrach and H. Miao, Convective heat transfer augmentation in thermal entrance regions by means of thermal instability, *J. Heat Transfer* **101**, 222–226 (1979).
10. K. C. Chiu and F. Rosenberger, Mixed convection between horizontal plates—I. Entrance effects, *Int. J. Heat Mass Transfer* **30**, 1645–1654 (1987).
11. K. C. Chiu, J. Ouazzani and F. Rosenberger, Mixed convection between horizontal plates—II. Fully developed flow, *Int. J. Heat Transfer* **30**, 1655–1662 (1987).
12. M. T. Ouazzani, J. P. Caltagirone, G. Meyer and A. Mojtabi, Etude numérique et expérimental de la convection mixte entre deux plans horizontaux, *Int. J. Heat Mass Transfer* **32**, 261–269 (1989).
13. M. T. Ouazzani, J. K. Platten and A. Mojtabi, Etude expérimental de la convection mixte entre deux plans horizontaux à températures différents—II, *Int. J. Heat Mass Transfer* **33**, 1417–1427 (1990).
14. D. G. Osborne and F. P. Incropera, Laminar, mixed convection heat transfer for flow between horizontal parallel plates with asymmetric heating, *Int. J. Heat Mass Transfer* **28**, 207–217 (1985).
15. D. G. Osborne and F. P. Incropera, Experimental study of mixed convection heat transfer for transitional and turbulent flow between horizontal, parallel plates, *Int. J. Heat mass Transfer* **28**, 1337–1344 (1985).
16. F. P. Incropera, A. L. Knox and J. A. Schutt, Onset of thermally driven secondary flow in horizontal rectangular ducts, *Proceedings of the eighth International Heat Transfer Conference*, San Francisco, pp. 1395–1400 (1986).
17. F. P. Incropera, A. L. Knox and J. R. Maughan, Mixed-convection flow and heat transfer in the entry region of a horizontal rectangular duct, *J. Heat Transfer* **109**, 434–439 (1987).
18. J. R. Maughana and F. P. Incropera, Experiments on mixed convection heat transfer for airflow in a horizontal and inclined channel, *Int. J. Heat Transfer* **30**, 1307–1318 (1987).
19. J. R. Maughan and F. P. Incropera, Regions of Heat transfer enhancement for laminar mixed convection in a parallel plate channel, *Int. J. Heat Mass Transfer* **33**, 555–570 (1990).
20. W. Nakakyama, G. J. Hwang and K.C. Cheng, Thermal instability in plane poiseuille flow, *J. Heat Transfer* **92**, 61–68 (1970).
21. G. J. Hwang and K. C. Cheng, Convective instability in the thermal entrance region of a horizontal parallel-plate channel heated from below. *J. Heat Transfer* **95**, 72–77 (1973).
22. F. S. Lee and G. J. Hwang, Transient analysis on the onset of thermal instability in the thermal entrance region of a horizontal parallel plate channel, *J. Heat Transfer* **113**, 363–370 (1991).

23. K. C. Cheng and G. J. Hwang, Numerical solution for combined free and forced laminar convection in horizontal rectangular channels, *J. Heat Transfer* **91,** 59–66 (1969).
24. K. C. Cheng, S. W. Hong and G. J. Hwang, Buoyancy effects on laminar heat transfer in the thermal entrance region of horizontal rectangular channels with uniform wall heat flux for large Prandtl number fluid, *Int. J. Heat Mass Transfer* **15,** 1819–1836 (1972).
25. J. W. Ou, K. C. Cheng and R. C. Lin, Natural convection effects on Graetz problem in horizontal rectangular channels with uniform wall temperature for large Pr, *Int. J. Heat Mass Transfer* **15,** 835–843 (1974).
26. K. C. Cheng and J. W. Ou, Convective instability and finite amplitude convection in the thermal entrance region of horizontal rectangular channels heated from below, *Proceedings of the seventh International Heat Transfer Conference*, Munish, Germany, paper NC-12, pp. 189–194 (1982).
27. K. C. Cheng and J. W. Ou, Buoyancy and tilt angle effects on Graetz problem in horizontal rectangular channels, *Proceedings of ASME–JSME Joint Conference on Thermal Engineering*, Vol. 3, pp. 141–147 (1983).
28. F. C. Chou and G. J. Hwang, Vorticity–velocity method for the Graetz problem and the effect of natural convection in a horizontal rectangular channel with uniform wall heat flux, *H. Heat Transfer* **109,** 704–710 (1987).
29. G. J. Hwang and F. C. Chou, Effect of wall conduction on combined free and forced laminar convection in horizontal rectangular channels, *J. Heat Transfer* **109,** 936–942 (1987).
30. F. C. Chou and W. Y. Lien, Effect of wall heat conduction on laminar mixed convection in the thermal entrance region of horizontal rectangular channels, *Wärmeund Soffübertragung* **26,** 121–127 (1991).
31. J. M. Huang, J. D. Lin and F. C. Chou, Combined radiation and laminar mixed convection in the thermal entrance region of horizontal isothermal rectangular channels, *Numer. Heat Transfer* **18,** 113–125 (1990).
32. F. P. Incropera and J. A. Schutt, Numerical simulation of laminar mixed convection in the entrance region of horizontal rectangular ducts, *Numer. Heat Transfer* **8,** 707–729 (1985).
33. H. V. Mahaney, F. P. Incropera and S. Ramadhyani, Development of laminar mixed convection flow in a horizontal rectangular duct with uniform bottom heating, *Numer. Heat Transfer* **12,** 137–155 (1987).
34. H. V. Mahaney, F. P. Incropera and S. Ramadhyani, Effect of wall heat flux distribution on laminar mixed convection in the entrance region of a horizontal rectangular duct, *Numer. Heat Transfer* **13,** 427–450 (1988).
35. H. V. Mahaney, S. Ramadhyani and F. P. Incropera, Numerical simulation of three-dimensional mixed convection heat transfer from an array of discrete heat sources in a horizontal rectangular duct, *Numer. Heat Transfer* **16,** 267–286 (1989).
36. J. R. Maughan and F. P. Incropera, Fully developed mixed convection in a horizontal channel heated uniformly from above and below, *Numer. Heat Transfer* **17,** 417–430 (1990).
37. C. C. Huang and T. F. Lin, Buoyancy induced flow transition in mixed convective flow of air through a bottom heated horizontal rectangular duct, *Int. J. Heat Mass Transfer* **37,** 1235–1255 (1994).
38. H. K. Moffat and K. F. Jensen, Complex flow phenomena in MOCVD reactors, *J. Crystal Growth* **77,** 108–119 (1986).
39. H. K. Moffat and K. F. Jensen, Three-dimensional flow effects in silicon CVD in horizontal reactors, *J. Electron-Chem. Soc.* **135,** 459–471 (1988).
40. R. K. Shah and A. L. London, *Laminar Flow Force Convection in Ducts*, pp. 196–198. Academic Press, New York (1978).
41. S. J. Kline and F. A. McClintock, Describing uncertainties in single-sample experiments, *Mech. Engng* **75,** 3–12 (1953).
42. T. A. Nyce, J. Ouazzani, A. Durand-Daubin and F. Rosenberger, Mixed convection in a horizontal rectangular channel-experimental and numerical velocity distributions, *Int. J. Heat Mass Transfer* **35,** 1481–1494 (1992).